

Direct Numerical Simulation of a Divergent Nozzle with Grid Transformation and Block Structure Mesh

Ryan Dunn*

University of California San Diego, San Diego, CA, 92093

I. Introduction

A divergent nozzle is a tube that is designed to accelerate choked flow ($M = 1$) to a supersonic flow. Often used in unison with a converging nozzle, the divergent nozzle is a critical component to the de Laval nozzle (also called the convergent-divergent nozzle). Diverging nozzles are a key component to the propulsion systems used in rocket engines and turbo jets. Maximizing the efficiency of a divergent nozzle is a problem that requires precise simulations to optimize the design. This includes turbulent mixing of gases, flow conditions along the interior surface of the nozzle, and the formation of shock waves in and around the divergent nozzle.

Properties of divergent nozzles are well understood and analytical solutions to basic properties of the flow exist [1, 2], however local solutions to the flow field are needed for higher fidelity analysis. High fidelity solutions give designers greater insight on the performance of divergent nozzles on a local level. Local flow solutions give insight to shock waves, expansion waves, downstream exhaust, and temperature fields. Thus, there exists a need to simulate the flow through a divergent nozzle with computational fluid dynamic simulators to analyze shock waves, exhaust characteristics, and conditions along the interior surface of the nozzle.

State of the art simulations for divergent nozzles can be done in commercial software such as ANSYS Fluent. Using ANSYS Fluent, Karandikar et al. [3] was able to capture complex internal shocks, expansion waves, flow separations, and small scale effects within the nozzle. Das et al. [4] analyzes the properties of normal shocks within the nozzle, and was able to achieve good agreement with theoretical predictions. Hunter [5] performed experiments with separated nozzle flows and was able to image local flow using Schlieren flow visualizations. While his work is dated, the contribution at the time showed that peak thrust efficiency could be improved with controlled flow separation from their experimental results. Thus, flow field solutions from both CFD and experiments are important to improving the performance of divergent nozzles.

The aim of this work is to simulate the acceleration of supersonic flow through the divergent section of a de Laval nozzle and capture the expansion waves in the exhaust region. Since analytic solutions to the velocity, temperature, and pressure distributions within the nozzle exist, we are able to directly compare the CFD solutions with the analytical solutions.

This work is built off of pre-existing code from the Midterm project, which simulates supersonic flow over a flat plate. Two major features have been added to this code: (1) The code has been modified to perform a grid transformation to a divergent nozzle, and (2) The code has been expanded by adding block structure to the mesh, which connects the divergent nozzle to the mesh blocks for the exhaust. All components of this project are done through MATLAB.

An outline of this project is presented here. Section II goes over the governing equations that characterize the flow of this problem. Section III presents the numerical methods to solve the equations. Section IV presents the model setup. Section V outlines the simulation results and validation to the divergent nozzle mode. Section VI discusses these results, their interpretation, and limitations to the model.

II. Governing Equations

This section gives an overview to the governing equations of the flow, as well as the analytical equations that characterize the flow through a de Laval nozzle.

At a high level, the simulation is solving for the x-velocity (u), y-velocity (v), temperature (T), pressure (p), and density (ρ) distribution in the flow field. To solve for these unknowns, we introduce the governing equations of the flow. Since we are in a supersonic flow regime, compressibility effects are non-negligible. Thus, we use the differential form

*Master's Student, Department of Mechanical and Aerospace Engineering, rdunn@ucsd.edu, A1560085

of the continuity equation in conservation form

$$\frac{\partial \rho}{\partial t} + \nabla \cdot (\rho \vec{u}) = 0. \quad (1)$$

The simulation uses of the momentum equations in both the x- and y-directions

$$\frac{\partial(\rho u)}{\partial t} + \nabla \cdot (\rho u \vec{u}) = -\frac{\partial p}{\partial x} + \frac{\partial \tau_{xx}}{\partial x} + \frac{\partial \tau_{yx}}{\partial y} + \rho f_x, \quad (2)$$

$$\frac{\partial(\rho v)}{\partial t} + \nabla \cdot (\rho v \vec{u}) = -\frac{\partial p}{\partial y} + \frac{\partial \tau_{yy}}{\partial y} + \frac{\partial \tau_{xy}}{\partial x} + \rho f_y, \quad (3)$$

where τ is the shear stress component in a given plane and direction and f is the forcing the terms in the corresponding direction.

Energy is also conserved in the flow. The energy equation in differential conservation form is

$$\begin{aligned} \frac{\partial E_t}{\partial t} + \nabla \cdot (E_t \vec{u}) = & \underbrace{\rho \dot{q}}_{\text{volumetric heating}} - \underbrace{\frac{\partial \dot{q}_x}{\partial x} - \frac{\partial \dot{q}_y}{\partial y}}_{\text{thermal conduction}} - \underbrace{\frac{\partial(Up)}{\partial x} - \frac{\partial(vp)}{\partial y}}_{\text{work done by pressure}} \\ & + \underbrace{\frac{\partial(u\tau_{xx})}{\partial x} + \frac{\partial(v\tau_{yy})}{\partial y}}_{\text{work done by normal stresses}} + \underbrace{\frac{\partial(u\tau_{xy})}{\partial y} + \frac{\partial(v\tau_{xy})}{\partial x}}_{\text{work done by shear stresses}} + \underbrace{u\rho f_x + v\rho f_y}_{\text{work done by body forces}}. \end{aligned} \quad (4)$$

To impose full closure on this system of equations, we must also impose additional relationships tabled in Table 1.

Table 1 Closure equations

Assumption/Definition	Equation	Assumption/Definition	Equation
Total energy	$E_t = \rho \left(\underbrace{e}_{\text{internal}} + \underbrace{\frac{u^2 + v^2}{2}}_{\text{kinetic}} \right)$	Fourier's Law	$\dot{q}_x = -\frac{\partial T}{\partial x}, \quad \dot{q}_y = -\frac{\partial T}{\partial y}$
Newtonian Fluid	$\tau_{xx} = 2\mu \left(\frac{\partial u}{\partial x} - \frac{1}{3} \nabla \cdot \vec{u} \right)$ $\tau_{xy} = \tau_{yx} = \mu \left(\frac{\partial v}{\partial x} + \frac{\partial u}{\partial y} \right)$	Constant Prandtl number	$k = \left(\frac{C_p}{Pr} \right) \mu$
Ideal Gas	$p = \rho RT$	Sutherland's Law	$\mu = \mu_0 \left(\frac{T}{T_0} \right)^{3/2} \frac{T_0 + S_1}{T + S_1}$
		Calorically perfect gas	$e = C_v T$

In total, the continuity (Eq. 1), momentum (Eqs. 2, 3), and energy (Eq. 4) equations can be combined into column vector form as in

$$\underbrace{\frac{\partial U}{\partial t}}_{\text{solution vector}} + \underbrace{\frac{\partial E}{\partial x} + \frac{\partial F}{\partial y}}_{\text{flux vectors}} = \underbrace{J}_{\text{source vector}}, \quad (5)$$

which has derivatives with respect to spatial coordinates. To solve this equation, the model must be discretized into a grid of points. For simple models, the grid of points are equally spaced and represent a simple rectangular domain. This makes the derivatives easy calculate with finite difference methods. However, when a more complex spatial domain is to be represented, a grid transformation is required to transform the rectangular grid to a more complex domain.

A. Isentropic Flow Equations

The flow distribution of a divergent nozzle can be written with analytic equations. The expected solution along the center-line of the divergent nozzle is expected to follow these characteristic equations. Near the no-slip boundaries,

these equations are not valid. These equations are valid for large Reynolds numbers, isentropic, steady, and ideal gas assumptions. The standard compressible, isentropic flow equations are given as

$$\frac{T_0}{T} = \left(\frac{P_0}{P} \right)^{\frac{\gamma-1}{\gamma}} = 1 + \frac{\gamma-1}{2} M^2 \quad (6)$$

$$\frac{A^*}{A} = M \left(\frac{2}{\gamma+1} \left(1 + \frac{\gamma-1}{2} M^2 \right) \right)^{-\frac{\gamma+1}{2(\gamma-1)}} \quad (7)$$

$$M = \frac{u}{\sqrt{\gamma R T}} \quad (8)$$

where T_0 is stagnation temperature, P_0 is stagnation pressure, γ is the specific heat capacity, and A^* is the critical area where the flow becomes choked. Ideally, A^* is the area of the throat of the CD nozzle.

Two critical locations arise in our flow. The first location is the throat, where $A = A_t = A^*$. The second critical location is the exit of the nozzle. The corresponding equations for these locations are tabled in Table 2.

Table 2 Throat and Exit state equations

Throat ($A = A_t$)	Exit ($A = A_e$)
$M_t = 1$	$\frac{A_t}{A_e} = M_e \left(\frac{2}{\gamma+1} \left(1 + \frac{\gamma-1}{2} M_e^2 \right) \right)^{-\frac{\gamma+1}{2(\gamma-1)}}$
$T_t = T_0 \left(\frac{2}{\gamma+1} \right)$	$T_e = T_0 \left(1 + \frac{\gamma-1}{2} M_e^2 \right)^{-1}$
$P_t = P_0 \left(\frac{2}{\gamma+1} \right)^{\frac{\gamma}{\gamma-1}}$	$P_e = P_0 \left(1 + \frac{\gamma-1}{2} M_e^2 \right)^{-\frac{\gamma}{\gamma-1}}$

Extending beyond the isentropic flow equations, we can also characterize the expansion waves. Expansion waves occur in the exhaust of the nozzle when the flow is under-expanded, when $P_e > P_a$. As the supersonic flow reaches atmosphere, it creates expansion waves, accelerating and deflecting the flow in order to match atmospheric pressure. The deflection angle θ can be calculated using the Prandtl-Meyer function (ν). Consider the initial Mach number M_1 and the Mach number after the turn M_2 . Then, the deflection angle is calculated by

$$\theta = \nu(M_2) - \nu(M_1), \quad (9)$$

$$\nu(M) = \sqrt{\frac{\gamma+1}{\gamma-1}} \arctan \sqrt{\frac{\gamma-1}{\gamma+1} (M^2 - 1)} - \arctan \sqrt{M^2 - 1}. \quad (10)$$

While isentropic flow equations provide a good solution to the center-line flow, additional validation is needed for the simulation. Thus, the 2D flow reconstruction will be compared to an existing MATLAB script which solves for a diverging nozzle flow [6]. This code was written during Britton Olson's Ph.D. candidacy in 2009. The script out-of-box generates a mesh of the diverging section of a nozzle, initializes a supersonic flow, and solves the same governing equations as in equation 5. The characteristic difference between the code presented and Olson's code is that the method presented in this paper is a direct-numerical simulation, whereas Olson's code using the Finite Volume Method (FVM).

III. Numerical Methods

This section introduces the numerical methods to solve equation 5 in a second order accurate way in both time and space. The methods for calculating the grid transformation are also shown.

An outline of finite difference methods is tabled in Table 3.

A grid transformation is a mapping from a rectangular grid to a complex spatial grid $\Phi : (\xi, \eta) \rightarrow (x, y)$. The grid transformation of equation 5 is represented as

$$\frac{\partial}{\partial t} \underbrace{(\mathcal{J}U)}_{\mathcal{U}} + \frac{\partial}{\partial \xi} \underbrace{(y_\eta E - x_\eta F)}_{\mathcal{E}} + \frac{\partial}{\partial \eta} \underbrace{(-y_\xi E + x_\xi F)}_{\mathcal{F}} = 0, \quad (11)$$

where \mathcal{J} is the grid transform jacobian, (x_η, y_η) are the spatial derivatives with respect to η , and (x_ξ, y_ξ) are the spatial derivatives with respect to ξ . The set of derivatives $(x_\eta, y_\eta, x_\xi, y_\xi)$ are called the inverse metrics. In some instances, the

Table 3 Finite difference methods for derivatives

Method	Equation (Truncation Error)
Euler Explicit	$\frac{\partial \phi}{\partial t} \approx \frac{\phi^{n+1} - \phi^n}{\Delta t} + O(\Delta t)$
Forward Difference	$\frac{\partial \phi}{\partial x} \approx \frac{\phi_{i+1} - \phi_i}{\Delta x} + O(\Delta x)$
Backward Difference	$\frac{\partial \phi}{\partial x} \approx \frac{\phi_i - \phi_{i-1}}{\Delta x} + O(\Delta x)$
Central Difference	$\frac{\partial \phi}{\partial x} \approx \frac{\phi_{i+1} - \phi_{i-1}}{2\Delta x} + O(\Delta x^2)$

mapping Φ can be analytic and have exact derivatives. In practice and in this project, the inverse metrics are calculated by finite difference.

At a high level, we solve equation 11 with MacCormack's method [7]. MacCormack's method uses a Euler explicit time scheme that consists of a predictor step using forward differences and a corrector step using backward differences of the derivatives. These two steps appear as

$$\overline{\mathcal{U}}_{i,j}^{n+1} = \mathcal{U}_{i,j}^n - \Delta t \left(\frac{\mathcal{E}_{i+1,j}^n - \mathcal{E}_{i,j}^n}{\Delta \xi} \right) - \Delta t \left(\frac{\mathcal{F}_{i,j+1}^n - \mathcal{F}_{i,j}^n}{\Delta \eta} \right) \quad (12)$$

$$\mathcal{U}_{i,j}^{n+1} = \frac{1}{2} \left(\mathcal{U}_{i,j}^n + \overline{\mathcal{U}}_{i,j}^{n+1} \right) - \frac{\Delta t}{2} \left(\frac{\overline{\mathcal{E}}_{i,j}^{n+1} - \overline{\mathcal{E}}_{i-1,j}^{n+1}}{\Delta \xi} \right) - \frac{\Delta t}{2} \left(\frac{\overline{\mathcal{F}}_{i,j}^{n+1} - \overline{\mathcal{F}}_{i,j-1}^{n+1}}{\Delta \eta} \right) \quad (13)$$

where equation 12 is the predictor step and equation 13 is the corrector step. This integration scheme is second order accurate.

In order to maintain second order accuracy, the derivatives within \mathcal{E} and \mathcal{F} must be carefully inspected. Since the corrector and predictor steps introduce bias in a certain direction, the spatial derivatives within \mathcal{E} and \mathcal{F} must oppose the direction of bias. For example, the temperature gradient within the energy equation $\frac{\partial T}{\partial \xi}$ has a bias in the ξ direction. Since the corrector step has a forward difference bias in ξ , $\frac{\partial T}{\partial \xi}$ is calculated with a backward difference scheme. Derivatives in η in this case have no bias, thus can be calculated with the second order accurate central difference scheme. The logic of this is outlined in the Figure 1.

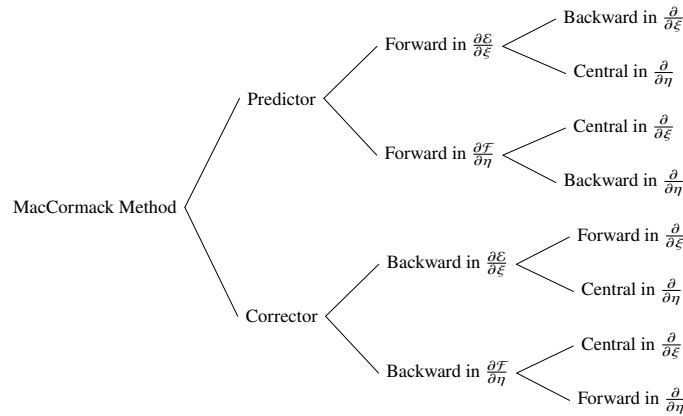


Fig. 1 Finite difference methods used for the partial derivatives in MacCormack's method.

In order to calculate equation 11, the inverse metrics must be calculated. The inverse metrics $(x_\xi, x_\eta, y_\xi, y_\eta)$ are calculated via finite difference as in Table 3. Then, using the determinant of the Jacobian (\mathcal{J}) the metrics $(\xi_x, \xi_y, \eta_x, \eta_y)$ can be calculated. This step can be interpreted as taking the the best linear approximation of the mapping

$f : (\xi, \eta) \rightarrow (x, y)$. The metric conversion equations are

$$\begin{aligned}\xi_x &= \frac{1}{J} y_\eta, & \eta_x &= -\frac{1}{J} y_\xi \\ \xi_y &= -\frac{1}{J} x_\eta, & \eta_y &= \frac{1}{J} x_\xi\end{aligned}\tag{14}$$

and the conversion to spatial derivatives are done by

$$\begin{aligned}\frac{\partial}{\partial x}(\cdot) &= \xi_x \frac{\partial}{\partial \xi}(\cdot) + \eta_x \frac{\partial}{\partial \eta}(\cdot) \\ \frac{\partial}{\partial y}(\cdot) &= \xi_y \frac{\partial}{\partial \xi}(\cdot) + \eta_y \frac{\partial}{\partial \eta}(\cdot)\end{aligned}\tag{15}$$

IV. Model Setup

This section gives an overview of the model setup. The mesh discretization is presented, both for the grid transformation and block structure mesh. The model is also outlined with key boundary conditions and initial conditions to ensure steady state flow is reached.

An important model assumption is that the 2D flow being simulated represents an infinitely long 3D nozzle. In reality, most nozzles are circular in their exit area, thus the area grows quadratically with respect to the increase in nozzle cross-sectional height. With the infinitely long nozzle assumption, we have a linear relationship between the cross-sectional height and the area. Thus, the height of the nozzle is considered as area per unit length of the nozzle.

Another critical model assumption is the inlet flow conditions of the divergent nozzle. Since we are neglecting the converging region of the de Laval nozzle, the developing boundary layer is not captured by the inlet conditions. As a result, the boundary layer within the divergent nozzle is not accurate when considering the full de Laval nozzle. The solution near the center-line of the divergent nozzle is considered to be accurate.

For simplicity, the working fluid in this problem is standard air. The properties of standard air and standard atmosphere are outlined in Table 4.

Table 4 Properties of standard air and standard atmosphere

Property	Value	Property	Value
Specific heat ratio (γ)	1.4	Specific heat volume (C_v)	718
Specific heat pressure (C_p)	1005	Gas constant (R)	287
Std. Pressure (P_a)	1.013×10^5 [Pa]	Std. Temperature (T_a)	288.15 [K]
Std. Density (ρ_a)	$1.225 \left[\frac{\text{kg}}{\text{m}^3} \right]$		

A. Grid Transformation

The spatial discretization of a divergent nozzle is obtained using the Method of Characteristics. The method of characteristics is a method of finding the characteristic lines associated with the fluid flow based on the PDE 11. The outer characteristic lines describe the walls of a diverging nozzle that does not expand too quickly or too slowly. A MATLAB implementation of this was found from Olson [6]. The implementation using the inflow conditions and throat height geometry, and then produces the maximum thrust, minimum length diverging nozzle discretization. This is done by finding the ideal area of the divergent nozzle, then choosing the ideal exit mach number to find the ideal exit area of the nozzle.

The parametric grid is a uniform rectangular grid. To optimize the conditioning of the Jacobian, the domain of the parametric space is the bounding box of the spatial domain. Figure 2 illustrates the parametric coordinates and spatial coordinates that it maps to for a divergent nozzle.

B. Block Structure

The next step to creating a discretization of our model is developing a block structured mesh. The block structure is essentially stitching together meshes and enforcing connectivity and communication between the blocks during

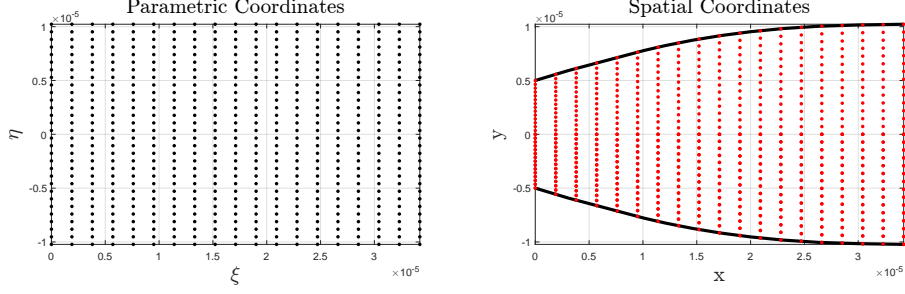


Fig. 2 Transformation of a uniform grid to an ideal diverging nozzle: ($A_t = 10^{-6}m$, $P_0 = 1.2 \times 10^6 Pa$)

the simulation. To simplify this, we consider a block structure where the blocks are both rectangular with uniformly distributed nodes that have equal spacing across blocks. The connection between two blocks is visualized in Figure 3. To ensure that the blocks communicate with one another, the ghost layer approach was implemented. The ghost layer approach operates by enforcing boundary conditions on each block such that there exists a ghost layer that is equivalent to the connecting block. The ghost layer is not physically part of the block, but is used to enforce the connection with its neighboring block. In Figure 3, the ghost layer of block 1 is the right intersecting column, and the ghost layer of block 2 is the left intersecting column. In practice, the ghost layers are implemented using modified boundary conditions on each block.

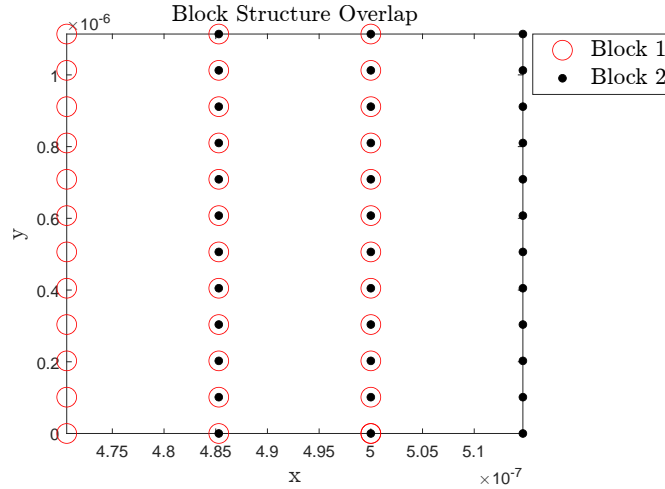


Fig. 3 Overlap between blocks

In summary, the grid transformation and block structure are combined into one mesh and simulated. The complete mesh layout is shown in Figure 4. In total, there are 4 blocks with 3 interfaces between the blocks. The ghost layer is applied to all 3 interfaces.

C. Boundary Conditions

To setup the problem, the model must be defined with appropriate boundary conditions. The following boundary conditions are applied to the mesh:

Choked Flow: The leftmost column in the nozzle is at $M = 1$, also called choked flow. The boundary conditions are considered to have reached sonic conditions. Using the FVM solver from Olson [6], the geometry is constructed for $P_0 = 1.2 \times 10^6 Pa$ and $T_0 = 2000K$. These are considered as ideal conditions, so the ideal simulation will be at this condition. However, some parameter study will be made varying the stagnation pressure P_0 . The resulting choked flow conditions for the ideal case are calculated from the equations in Table 2 and tabled in Table 5. Note that P_{CH} is the specific pressure condition for a supersonic jet where the exit pressure is theoretically equal to atmospheric ($p_e = p_a$). For $p > p_{CH}$, expansion waves are expected to form at the exhaust of the nozzle.

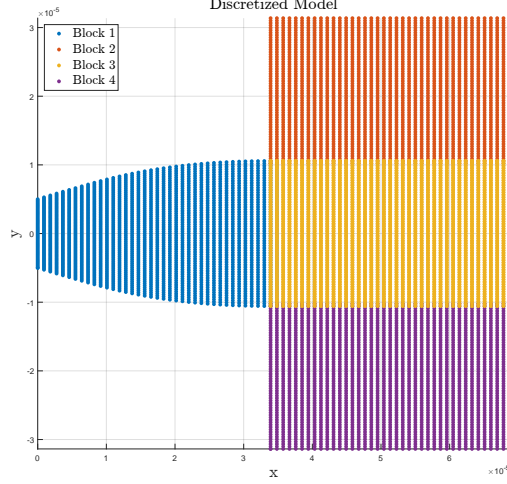


Fig. 4 Full model discretization visualization

Table 5 Choked flow for $P_0 = 1.2 \times 10^6 [Pa]$ and $T_0 = 2000 [K]$

Velocity	Value	Property	Value
u_{CH}	$818.38 \left[\frac{m}{s} \right]$	T_{CH}	$1667 [K]$
v_{CH}	$0 \left[\frac{m}{s} \right]$	P_{CH}	$6.340 \times 10^5 [Pa]$

No-Slip: No-slip wall conditions with extrapolated temperature and pressure are implemented for the walls of the nozzle. To maintain second order accuracy, a second order accurate extrapolation method is used as in

$$\phi_{i,1} = \frac{4\phi_{i,2} - \phi_{i,3}}{3} \quad (16)$$

Far Field: The far field conditions are considered to be in standard atmospheric conditions. The nozzle is considered to be on an aircraft flying at standard atmosphere sea-level conditions at near transonic conditions, $M = 1.5$.

Downstream: The rightmost boundary uses extrapolated velocity, pressure, and temperature values.

D. Initial Conditions

To initialize the full model in 4, an isolated simulation of the nozzle at operating conditions is first initialized. This excludes blocks 2, 3, and 4, and the exit flow conditions are extrapolated. For blocks 2 and 4 the far-field conditions are imposed as initial values. Block 3 is set to be a gradient between the exit conditions of the nozzle (block 2) and far-field conditions at the exit. An initialization of the nozzle is visualized in Figure 5.

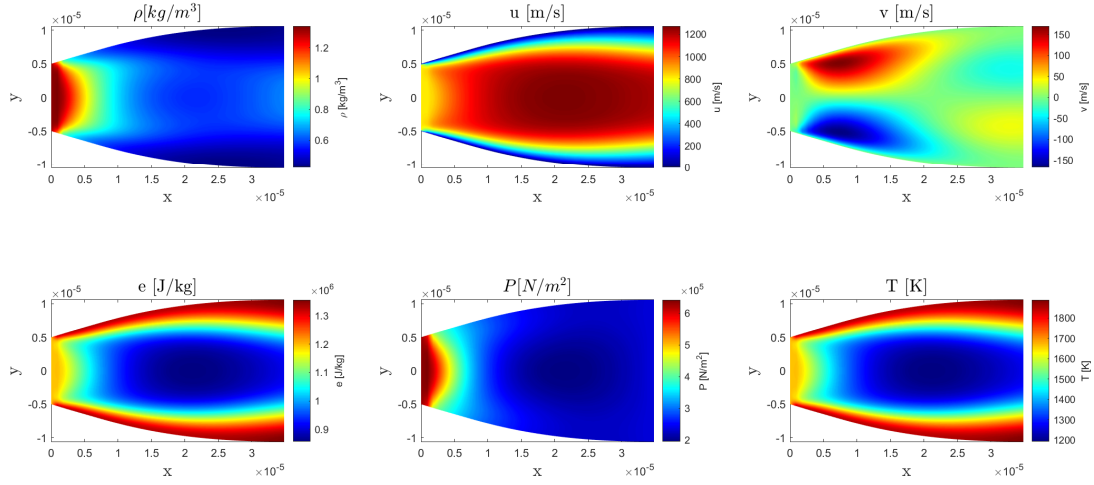


Fig. 5 Nozzle-only simulation used for initializing the full domain

V. Validation & Results

This section presents results from the simulation. Solutions are considered to be steady-state. Each block visualized in Figure 4 is (40×61) grid points. It should be noted that the main purpose of this simulation is not to capture high accuracy near the walls of nozzle. Instead, the focus of the work is on the centerline flow through the nozzle and its exit to atmospheric conditions. Higher resolution models will improve the boundary layer flow within the nozzle, however does not change the centerline flow properties, thus the model is considered to reach grid independence.

Simulations were ran at varying choked flow conditions (pressure variations only). The objective with varying the pressure is to observe under-expanded, supersonic jets, and over-expanded flows. Unfortunately, due to the sharp singularities pressure in oblique shocks, only supersonic jets and underexpanded flows were able to be simulated. As a benchmark, the nominal stagnation pressure was tested in the DNS code I created, and compared directly with the finite volume method used in Olson's code. Figure 6 visualizes the pressure and mach number distributions for the divergent nozzle between my implementation and Olson's code. The results from my code over-estimate pressure and under-estimate mach number. Most notably, my code captures the boundary layer within the nozzle's walls, so significant error in mach number is near the walls. Error in the pressure distribution occurs near the throat of the nozzle, when the most sudden height growth occurs. Room for improvement exists if the wall boundary conditions were changed. Because of the high pressure flow and low resolution, the model is likely over-predicting the boundary layer thickness. Despite these results, we will continue on in the analysis of the nozzle flow using the DNS implementation.

After initializing with the nozzle-only solution, the full model was ran. Due to the significant error in pressure, the expected inlet pressure for ideal nozzle flow were not reached unless the pressure inlet was reduced. Thus, a choice of $P = 0.75P_0$ was altered to the left boundary conditions such that the exit pressure of the simulated nozzle was near equal to ambient pressure. The results from this simulation are visualized in Figure 7. Two oblique shocks are captured along the top and bottom of the nozzle. This shock is because the far-field boundary conditions are $M = 1.5$ and the tip of the nozzle has an enforced no-slip condition. Additionally, the regions of large vertical velocity components v at the exit of the nozzle should be noted. The streamlines of this flow solution are shown in Figure 8. All streamlines in the exhaust are approximately straight, which is the expected result.

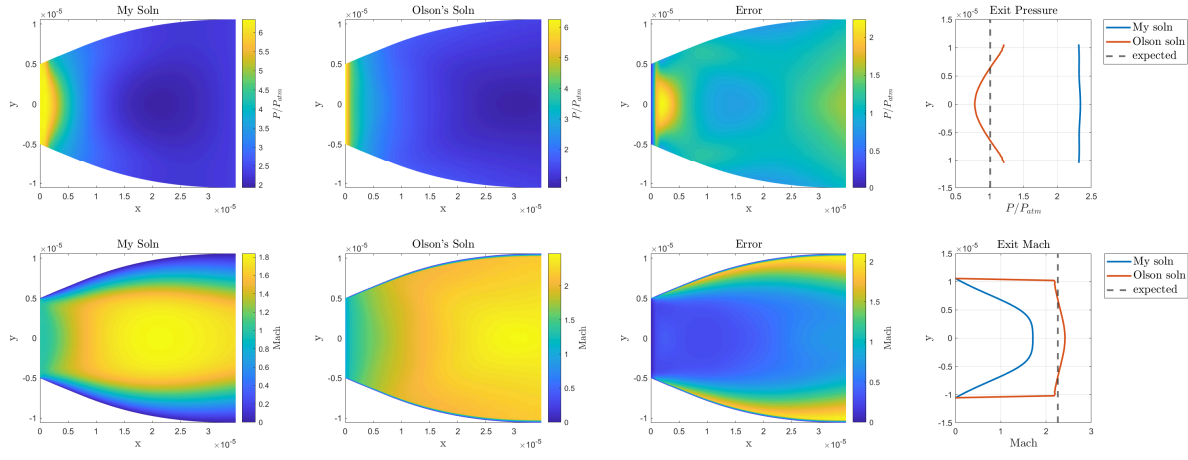


Fig. 6 Pressure and Mach number validation with Olson's finite volume method code

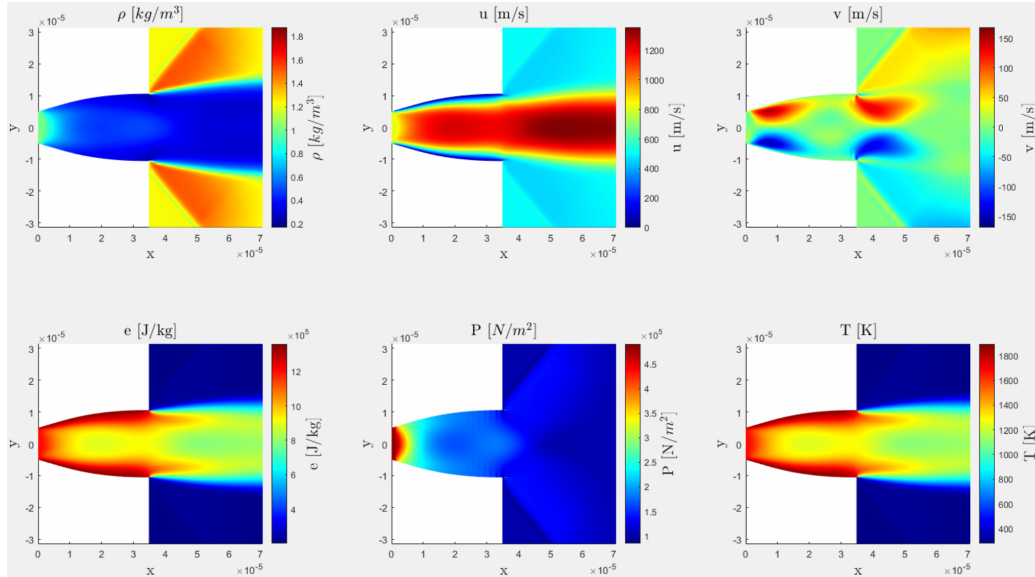


Fig. 7 Simulated ideal nozzle flow $P_e \approx P_{atm}$

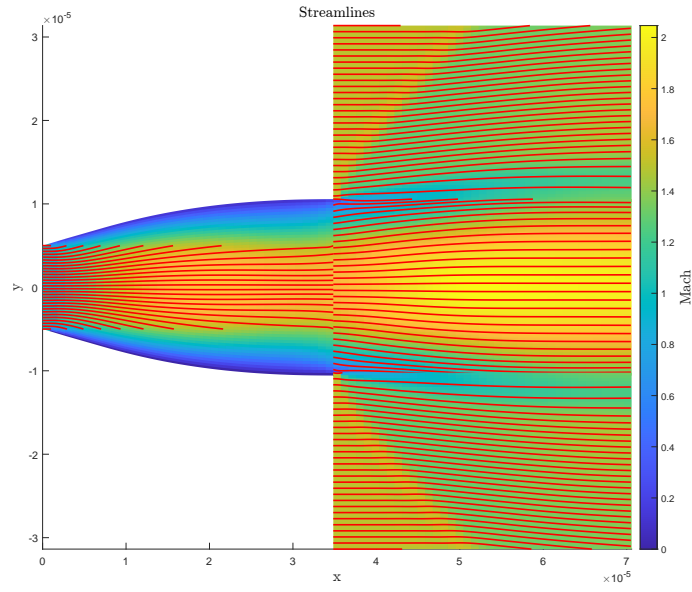


Fig. 8 Streamlines of the ideal nozzle flow $P_e \approx P_{atm}$

VI. Discussion

This section discusses the analysis of the nozzle flow model at non-ideal inlet conditions. The validation and results section illustrated the ideal nozzle flow where the inlet conditions produce an ideal case for which the outlet pressure is equal to ambient pressure. Now, we will apply higher inlet pressures to produce an underexpanded flow nozzle exhaust. Figure 9 illustrates the various exhaust flows produced by varying the inlet pressure P to its ideal inlet pressure P_0 . As pressure is increased, the simulation produces a resulting expansion of the downstream flow as it reaches atmospheric conditions. This phenomena of the downstream flow acceleration is a result of the expansion waves of the flow. As the pressure at the exit of the nozzle is increased, increasingly powerful expansion waves are produced that further accelerate and deflect the flow. The approximate deflection lines are indicated in Figure 9.

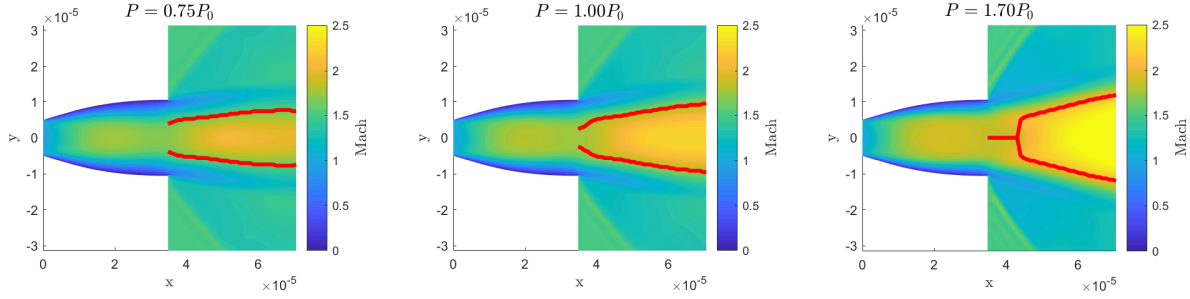


Fig. 9 Approximate deflection lines for varying inlet pressure conditions

Using the approximate deflection angles and the Prandtl-Meyer function 9, we can numerically calculate the expected deflection angle given the acceleration of the exhaust flow. The mach numbers at a given x coordinate of the exhaust can be measured two ways: (1) by the centerline or (2) by averaging the approximate supersonic exhaust region. Using either of these measurements contain numerical error and abstraction from the exact mach number distribution, however is needed to calculate deflection angles using the Prandtl-Meyer function. Additionally, an automated script measures the deflection angle observed in the simulation's solution. The results for both centerline mach numbers, average mach numbers, and the observed deflection angles are tabled in Table 6. The simulation produced an observable angle that falls between the numerical angles approximated by the centerline and average mach number of the exhaust. This is a success on the simulation, showing that the expansion wave angles observed are within theoretical expectations.

Table 6 Expansion Wave Angles in the Exhaust are not Accurate

		Exit Mach	Downstream Mach	Numerical Angle	Observed Angle
$P = 0.75P_0$	Centerline	1.71	1.99	8.09°	10.01°
	Average	1.32	1.73	11.94°	
$P = 1.0P_0$	Centerline	1.76	2.26	11.94°	16.65°
	Average	1.42	2.06	18.39°	
$P = 1.7P_0$	Centerline	1.85	2.69	21.36°	22.53°
	Average	1.58	2.57	26.48°	

The exit pressure distributions for three inlet pressure cases are visualized in Figure 10. As inlet pressure is increased, the exit pressures are subsequently increased. Additionally, higher pressure inlet conditions produce a greater difference between the centerline pressure and wall pressure of the nozzle. This is likely strongly linked to the wall pressure boundary conditions and no-slip wall condition. None of the three inlet conditions produce the theoretical exit pressures expected, nor match the code from Olson.

The centerline pressure and mach number distributions in the model are visualized in Figure 11. Pressure distribution after passing out of the exit of the nozzle smoothly drops to reach atmospheric pressure. Subsequently, the drop in pressure produces an increase in flow velocity. The mach number increases as a result. As discussed previously, this phenomena is observed to be the expansion waves in the exhaust of the nozzle.

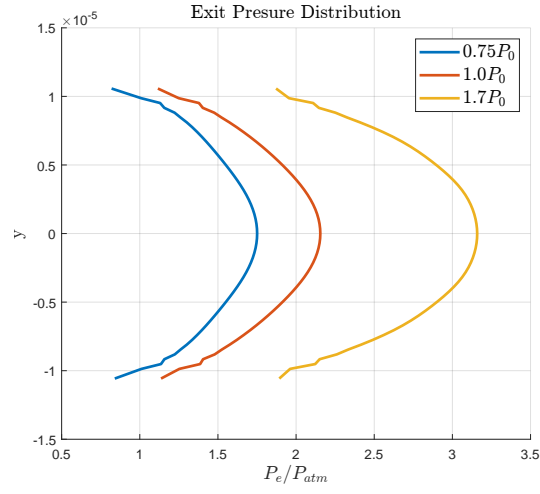


Fig. 10 Nozzle exit pressure distributions for varying inlet pressures

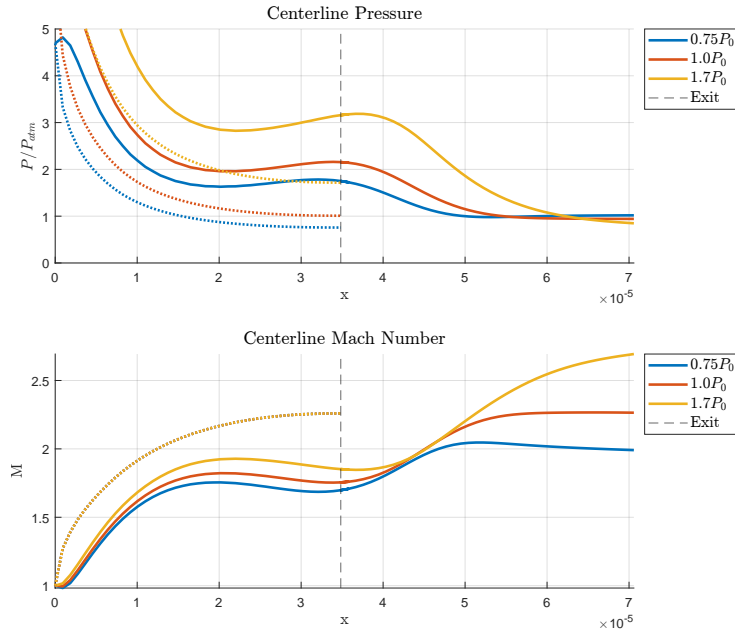


Fig. 11 Centerline pressure and mach number distributions varying inlet pressures compared to theory

VII. Conclusion

This paper presented a direct numerical simulation of a divergent nozzle with exhaust flow to atmosphere. The numerical formulation of the direct numerical simulation was presented to maintain second order accuracy in both time and space. A grid transformation and block structured mesh were introduced to previous work and applied to construct the model. After imposing boundary and initial conditions, the model was solved for ideal pressure inlet conditions and had high errors in pressure and mach number compared to theory and pre-existing code. Further, non-ideal pressure inlet conditions were simulated. Expansion waves in the underexpanded exhaust were observed and found to be within reasonable theoretical deflection angles. Exit pressure and centerline properties were observed.

A major limitation of this work is the large error for the ideal pressure inlet condition simulation. Large error may be due to wall boundary conditions, and it is recommended for future work to explore various wall boundary conditions within the nozzle to be imposed to decrease this error. In addition, overexpanded flow is not able to be resolved by this direct numerical simulator. Overexpanded flow contains boundary layer separation, recirculating flow, and intersecting oblique shocks within the nozzle that are not able to be solved by the formulation. Future work to explore methods and extensions to this simulator in order to capture overexpanded flow should be made. Another limitation of this approach is that the code implementation simulates a full model. However, the system is inherently symmetric. A significant decrease in computation time can be made if only half of the domain is simulated and a symmetrical boundary constraint is imposed.

References

- [1] Gerhart, P., Gerhart, A., and Hochstein, J., *Munson, Young and Okiishi's Fundamentals of Fluid Mechanics*, Wiley, 2016. URL <https://books.google.com/books?id=UBqRCgAAQBAJ>.
- [2] Antonio L. Sánchez, J. C. L., Adam Weiss, "An Introduction to Compressible Flow for Propulsion Applications," , December 2020.
- [3] Karandikar, R., Mishra, A., Kavipriya, J., and Kumar, A., "Study Of Nozzle Flow Separations In Divergent Section of Nozzle," *International Journal of Science and Engineering*, Vol. 07, 2021, pp. 29–38.
- [4] Das, B., Sardar, R., Sarkar, S., and Manna, N., *Compressible Flow Through Convergent–Divergent Nozzle*, 2021, pp. 345–353. doi:10.1007/978-981-33-4165-4_32.
- [5] Hunter, C. A., "Experimental Investigation of Separated Nozzle Flows," *Journal of Propulsion and Power*, Vol. 20, No. 3, 2004, pp. 527–532. doi:10.2514/1.4612, URL <https://doi.org/10.2514/1.4612>.
- [6] Olson, B., "2-D Nozzle Design," , 2009. URL <https://www.mathworks.com/matlabcentral/fileexchange/14682-2-d-nozzle-design>, mATLAB Central File Exchange; accessed May 22, 2022.
- [7] MacCormack, R. W., "The Effect of Viscosity in Hypervelocity Impact Cratering," *Journal of Spacecraft and Rockets*, Vol. 40, No. 5, 2003, pp. 757–763. doi:10.2514/2.6901, URL <https://doi.org/10.2514/2.6901>.